# Static and dynamic deformation mechanisms of a high-density polyethylene having row-nucleated crystalline texture of *a*-axis orientation as observed by orientation distribution function of crystallites*

**Kuniyasu Shiro†, Ken-ichi Fujita‡, Shoji Suehiro and Hiromichi Kawai§**
*Department of Polymer Chemistry, Faculty of Engineering, Kyoto University, Kyoto* 606, *Japan*
(*Received* 14 *October* 1982; *revised* 7 *December* 1982)

The rheo-optical properties of a high-density polyethylene having a row-nucleated crystalline texture of *a*-axis orientation were investigated in the machine direction (MD) and transverse direction (TD) of fabricating the specimen. The tensile complex dynamic compliance function $J^*$ displays two dispersions designated as the $\alpha_1$ and $\alpha_2$ mechanical retardation processes with activation energies of about 21 and 35 kcal mol$^{-1}$, respectively, for both MD and TD specimens, and the complex dynamic stress-optical coefficient function $M^*$ exhibits a single discrete dispersion designated as the $\alpha$ optical retardation process with an activation energy of about 24 kcal mol$^{-1}$ for both specimens over the same frequency and temperature ranges as those covered for the dynamic mechanical measurements. The real and imaginary components of $M^*$ converge from positive values to almost zero at the highest frequencies and lowest temperatures covered for both specimens, with the exception of the real component of the MD specimen which converges to a small but definitely negative value. The analysis of this anomalous behaviour of the MD specimen in terms of the optical retardation time spectrum has ascribed the negative convergence to a negative form birefringence that arises from a dynamic lamellar splaying or bending process responding in phase with the dynamic bulk stress. The dynamic X-ray diffraction studies have revealed the $\alpha$ optical dispersion and possibly the $\alpha$ mechanical dispersion to be mostly attributed to the crystal orientation dispersions involving intralamellar shearing processes, i.e. detwisting and tilting processes of the lamellar segments for the MD and TD specimens, respectively. The optical dispersion, if any, associated with the lamellar splaying or bending process may be expected at higher frequencies or lower temperatures than those covered here to assign the $\beta$ mechanical dispersion to the interlamellar shearing process.

**Keywords** Rheo-optical properties; row-nucleated high-density polyethylene; deformation mechanism of crystalline texture; $\alpha$ and $\beta$ mechanical dispersions; orientation distribution function of crystal grains; inter- and intra-lamellar crystal-grain-boundary phenomena

## INTRODUCTION

The dynamic mechanical properties of spherulitic polyethylene have been studied extensively by means of dynamic rheo-optical techniques to assign the $\alpha$ and $\beta$ mechanical dispersions to intra- and interlamellar crystal-grain-boundary phenomena[1-8]. However, the assignments are mostly based on the dynamic rheo-optical parameters, such as dynamic responses of the second-order orientation factors of crystalline and non-crystalline structural units, nothing but the second moments of orientation distribution functions of the structural units, thus still leaving some obscurity and speculation on the assignments.

In one of the previous papers of this series[9] the crystal orientation behaviour during stretching a spherulitic high-density polyethylene was observed in terms of uniaxial orientation distribution functions $q_j(\zeta_j,0)$ for 13 different crystal planes and, further, $w(\xi,0,\eta)$ for crystal grains (crystallites), both as a function of the extension ratio of bulk specimen up to a certain limiting ratio beyond which the macroscopic necking of the specimen develops. The uniaxial deformation mechanism of a polyethylene spherulite was discussed quantitatively by comparing the dependence of the function $w(\xi,0,\eta)$ upon the extension ratio with that calculated from a spherulite deformation model combining orientation of the crystal lamellae in affine fashion with reorientation of the crystal grains within the orienting lamellae. The crystal reorientation mechanism was represented by two preferential modes which involved rotations of the crystal

* Presented at the 30th Annual Meeting of the Society of Polymer Science, Japan, Kyoto, 28–30 May, 1981. This paper will be designated hereafter as part XV of 'Rheo-optical studies on the deformation mechanism of semicrystalline polymers'

† Present address: Toray Research Center, Sonoyama-cho, Otsu 520, Japan

‡ On leave from the Department of Polymer Engineering, Nagoya Institute of Technology, Gokisho, Showa-ku, Nagoya 466, Japan

§ To whom correspondence should be addressed

0032-3861/83/091113-15$03.00

grains about their own *a*- or *b*-axes so as to orient their *c*-axes (molecular axes) towards the stretching direction. The rotations of the crystal grains about the crystal *a*- or *b*-axes were accentuated in the polar or equatorial zones of the uniaxial deformation model of the spherulite, respectively, so as to achieve good agreement between the calculated and observed results.

The analysis of the spherulite deformation mechanism by use of the orientation distribution function of the crystal grains $w(\xi,0,\eta)$ is much more quantitative and straightforward[10-12], in general, than that in terms of the moments of the orientation distribution function of the *j*th crystal planes, such as the second moments[13-16], as mentioned above. Therefore, the analysis has been extended to the dynamic investigation of the spherulite deformation mechanism in order to confirm the assignments of the $\alpha$ and $\beta$ mechanical dispersions of spherulitic polyethylene[17]. That is, the investigation of the dynamic response of the crystal grains within the spherulites in terms of the complex dynamic orientation distribution function,

$$\Delta w^*(\xi,0,\eta)=\Delta w'(\xi,0,\eta)-i\Delta w''(\xi,0,\eta)$$

by means of an advanced dynamic X-ray diffraction technique[18]. The investigation has assured the assignments of the $\alpha$ and $\beta$ mechanical dispersions of spherulitic polyethylene to the intra- and interlamellar crystal-grain-boundary phenomena, i.e. the dynamic orientation dispersion of the crystal lamellae themselves and that of the crystal grains within the lamellae in association with the two types of preferential rotations of the grains about the crystal *a*- and *b*-axes at the polar and equatorial zones of the spherulites, respectively, all postulated on a basis of the uniaxial deformation model of the spherulite.

The specimen employed in the previous investigations was the isotropic melt-crystallized one possessing the spherulitic crystalline texture. The local strain at the equatorial zone of a uniaxially deformed spherulite is usually larger than that at the polar zone[19], reflecting crystalline topology and morphology of lamellar aggregation in the spherulitic texture of spherical symmetry. The time-dependent deformation behaviour is also different locally with respect to the angular position of the spherulite[20]. The rheo-optical responses available from the spherulitic specimen, such as optical absorption and emission dichroisms as well as X-ray diffraction, are usually averaged over all the azimuthal angles of the spherulite, thus leading to difficulties in resolving the optical responses into fundamental structural responses, if any, unless models of spherulite deformation are postulated.

The idea that is developed for overcoming the obscurity in resolving the optical responses from the spherulitic systems is to use a particular film specimen crystallized from stress melts of polyethylene which has a row-nucleated crystalline texture grown in cylindrical symmetry along the machine direction (MD) of fabricating the film specimen[21]. The specimen has cylindrites in which stacked crystal lamellae are oriented radially with their lamellar axes highly perpendicular to the machine direction. Therefore, the structural responses that occur for tensile deformation of the specimen along the machine direction may represent those expected at the equatorial zone of spherulitic texture, whereas the responses that occur for tensile deformation of the specimen along the transverse direction (TD) of fabrication may reflect the responses expected primarily at the polar zone of the spherulitic texture.

In this paper, the dynamic mechanical and optical (birefringence) behaviour of a film specimen crystallized from the stress melts of a relatively high molecular weight polyethylene possessing the row-nucleated crystalline texture of *a*-axis orientation will be investigated. The dynamic birefringence behaviour is discussed in conjunction with the dynamic crystal orientation behaviour obtained from the dynamic X-ray diffraction studies of the same material in order to explore the structural origins of the $\alpha$ mechanical dispersion of the row-nucleated specimen as well as isotropic melt-crystallized specimen of spherulitic texture.

## EXPERIMENTAL

### *Test specimen*

A relatively high molecular weight linear polyethylene (Sholex 4002L, Japan Olefin Chemical Ind., Ltd) having a weight-average molecular weight of $19.9\times10^4$ and a viscosity-average molecular weight of $14.1\times10^4$ was fed into a Bumbery mixer where the pellets were melted for several minutes. The melt kept at $\sim160$°C at the exit of the mixer was fed into mixing rolls controlled at 150°C and then calendered into a sheet by passing through a set of calender rolls, as shown schematically in *Figure 1*. The temperature and relative surface velocity of the rolls were controlled, as fully discussed elsewhere[22], so as to crystallize the melts under relatively high shear stress. That is, the temperatures of the first to third rolls in *Figure 1* were controlled at 170°C, and that of the fourth roll was controlled at 150°C, while the rest were controlled at ambient temperature. The friction ratios of the rolls were set so that the ratios of surface velocities of the first to the fourth rolls were 1:1.25:1.30:1.32. The surface velocity of the fourth roll was set at 5 m $min^{-1}$ and the film specimen was taken up at a velocity of 6 m $min^{-1}$. The calendered films thus prepared have a thickness of $\sim200$ $\mu$m and a density of 0.941 g $cm^{-3}$ from which the volume- and weight-averaged crystallinities are found as 63.9% and 60.2%, respectively, by assuming the densities of the crystalline and non-crystalline regions to be 1.000 and 0.852 g $cm^{-3}$, respectively.

### *Experimental procedure*

Prior to the static and dynamic experiments, the above-mentioned specimens were annealed by placing them between two polished stainless-steel plates at 110°C for more than 5 h in a vacuum oven in order to prevent undesirable thermal effects occurring during the experiments. For the dynamic mechanical and birefringence

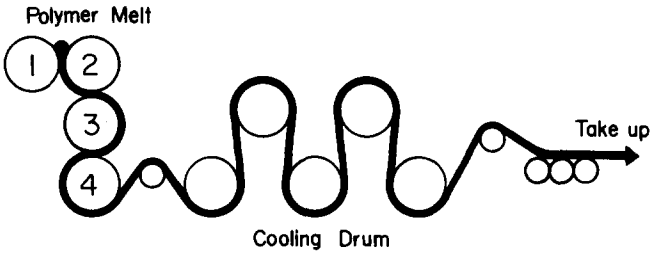


*Figure 1* Schematic diagram of calender process

experiments, the film specimen of ~200 $\mu$m thickness was cut into a ribbon shape of 80 mm length and 8 mm width along the machine and transverse directions, respectively, and were designated hereafter as the MD and TD specimens. For the static and dynamic X-ray diffraction experiments, the film specimen was cut into a ribbon shape of 100 mm length and 15 mm width and 60 mm length and 15 mm width, respectively, both only along the machine direction.

The ribbon shape specimen for the dynamic mechanical and birefringence measurements was mounted in a tensile dynamic deformation apparatus at an initial gauge length of 60 mm and was subjected to a static tensile strain of 3.3% to avoid buckling of the specimen when imposing a dynamic tensile strain of 0.25%. A preparatory vibration was applied for about 1 h at 4.3 Hz at each measuring temperature in order to assure a sort of mechanical conditioning of the specimen. The simultaneous measurement of dynamic mechanical and dynamic birefringence behaviour was conducted by means of a $\pi$-sector technique[23] over a frequency range from 0.0083 to 4.3 Hz at various temperatures from 10° to 100°C.

The ribbon shape specimen for the static X-ray diffraction measurement was mounted in a tensile stretching device at an initial gauge length of 80 mm and was stretched uniaxially at 60°C with a strain rate of 1.5% $min^{-1}$ up to extension ratios of 1.2 and 1.4 without any development of macroscopic necking of the specimens. The stretched specimens were clamped between two metallic flanges and kept at ambient temperature for about a week before the static X-ray diffraction measurement. The measurement was performed by using an ordinary horizontal scanning-type diffractometer in a fixed-time step-scanning manner over a range of twice the Bragg angle from 12° to 78° with 0.1° (or 1°) intervals and a range of azimuthal angles from 0° to 90° with 1° (or 5°) intervals to investigate the orientation distribution functions $q_j(\zeta_j,0)$ of 13 different ($j$th) crystal planes, as listed in *Table 1*.

The ribbon shape specimen for the dynamic X-ray diffraction measurement was mounted in another tensile dynamic deformation apparatus at an initial gauge length of 40 mm, further cut into thin strips of about 3 mm width along the gauge length to avoid biaxial deformation of the specimen, if any, and subjected to a static tensile strain of 3.0% superimposed on a dynamic tensile strain of 0.886%. The dynamic X-ray diffraction measurement was conducted by means of a multichannel narrow-sector technique[18] at three particular temperatures and frequencies: 25°C, 3.2 Hz; 50°C, 0.2 Hz; and 80°C, 0.2 Hz. The dynamic measurement was carried out by using a dynamic X-ray diffractometer[24] also in a fixed-time step-scanning manner over a range of twice the Bragg angle from 12° to 48.6° and a range of azimuthal angles from 0° to 90° to investigate the dynamic change of orientation distribution function of the $j$th crystal plane, $\Delta q_j^*(\zeta_j,0)$ for six different crystal planes, the (110), (200), (210), (020), (201), and (211) crystal planes, and further that of the crystallites (crystal grains), $\Delta w^*(\xi,0,\eta)$. The detailed procedure of the investigation of $\Delta q_j^*(\zeta_j,0)$ and $\Delta w^*(\xi,0,\eta)$ has been discussed fully elsewhere[9,17] and will be described as briefly as possible.

*Table 1* The $j$th crystal plane adopted and orientation of its reciprocal lattice vector $\mathbf{r}_j$ within the Cartesian coordinate system O–$u_1u_2u_3$

| Crystal plane | | $u_1 \parallel a$, $u_2 \parallel b$, $u_3 \parallel c$ | | $u_1 \parallel c$, $u_2 \parallel a$, $u_3 \parallel b$ | |
|---|---|---|---|---|---|
| ($hkl$) | $2\theta_B$ | $\Theta_j$ | $\Phi_j$ | $\Theta_j$ | $\Phi_j$ |
| (110) | 21.62 | 90.00 | 56.31 | 33.69 | 90.00 |
| (200) | 24.02 | 90.00 | 0.00 | 90.00 | 90.00 |
| (210) | 30.15 | 90.00 | 36.87 | 53.13 | 90.00 |
| (020) | 36.38 | 90.00 | 90.00 | 0.00 | – |
| (120) | 38.42 | 90.00 | 71.57 | 18.43 | 90.00 |
| (011) | 39.79 | 27.30 | 90.00 | 62.80 | 0.00 |
| (310) | 40.85 | 90.00 | 26.57 | 63.43 | 90.00 |
| (111) | 41.69 | 31.81 | 56.31 | 64.10 | 18.90 |
| (201) | 43.07 | 34.54 | 0.00 | 90.00 | 34.40 |
| (220) | 44.06 | 90.00 | 56.31 | 33.69 | 90.00 |
| (211) | 47.01 | 40.71 | 36.87 | 67.00 | 34.40 |
| (311) | 55.00 | 49.10 | 26.57 | 70.29 | 45.77 |
| (002) | 74.40 | 0.00 | – | 90.00 | 0.00 |

Unit is degrees

*Definition of complex dynamic orientation distribution function of crystallites and its investigation from dynamic X-ray diffraction*

*Figure 2a* specifies the orientation of a Cartesian coordinate system O–$u_1u_2u_3$ fixed within a crystallite (or crystal grain) with respect to another Cartesian coordinate system O–$x_1x_2x_3$ fixed within a bulk specimen in terms of three Euler angles, $\phi$, $\theta$ and $\eta$. *Figures 2b* and *2c* specify the orientation of a given vector $\mathbf{r}_j$ (reciprocal lattice vector of the $j$th crystal plane) within the crystallite and the bulk specimen, respectively, in terms of the polar and azimuthal angles, $\Theta_j$ and $\Phi_j$ and $\theta_j$ and $\phi_j$.

The orientation distribution functions of the crystallites and the $j$th vectors within the bulk specimen, $w(\theta,\phi,\eta)$ and $q_j(\theta_j,\phi_j)$, can be defined, respectively, under the following normalization conditions:

$$\int_{\eta=0}^{2\pi}\int_{\phi=0}^{2\pi}\int_{\xi=-1}^{1} w(\xi,\phi,\eta)\mathrm{d}\xi\,\mathrm{d}\phi\,\mathrm{d}\eta = 1 \tag{1}$$

$$\int_{\phi_j=0}^{2\pi}\int_{\zeta_j=-1}^{1} q_j(\zeta_j,\phi_j)\mathrm{d}\zeta_j\,\mathrm{d}\phi_j = 1 \tag{2}$$

where $\xi=\cos\theta$ and $\zeta_j=\cos\theta_j$.

For a particular combination of cylindrical symmetry of $q_j(\zeta_j,\phi_j)$ about the $x_3$ axis with orthorhombic symmetry of the Cartesian coordinate system O–$u_1u_2u_3$, which holds for the present study of uniaxial stretching of the calendered film of polyethylene along the machine direction, the orientation distribution functions can be expanded into infinite series, as discussed fully by Roe and Krigbaum[25–27]. Namely,

$$w(\xi,0,\eta)=\sum_{l=0}^{\infty}A_{l00}\Pi_l(\xi)+2\sum_{l=2}^{\infty}\sum_{n=2}^{l}A_{l0n}\Pi_l^n(\xi)\cos(n\eta) \tag{3}$$

$$q_j(\zeta_j,0)=\sum_{l=0}^{\infty}\alpha_{l0}^{j}\Pi_l(\zeta_j) \tag{4}$$

where $A_{lmn}$ and $\alpha_{lm}^j$ are real components of the coefficients of each expanded series, $\Pi_l^n(x)$ are normalized Jacobi polynomials, and $l$, $m$ and $n$ are integers indicating the

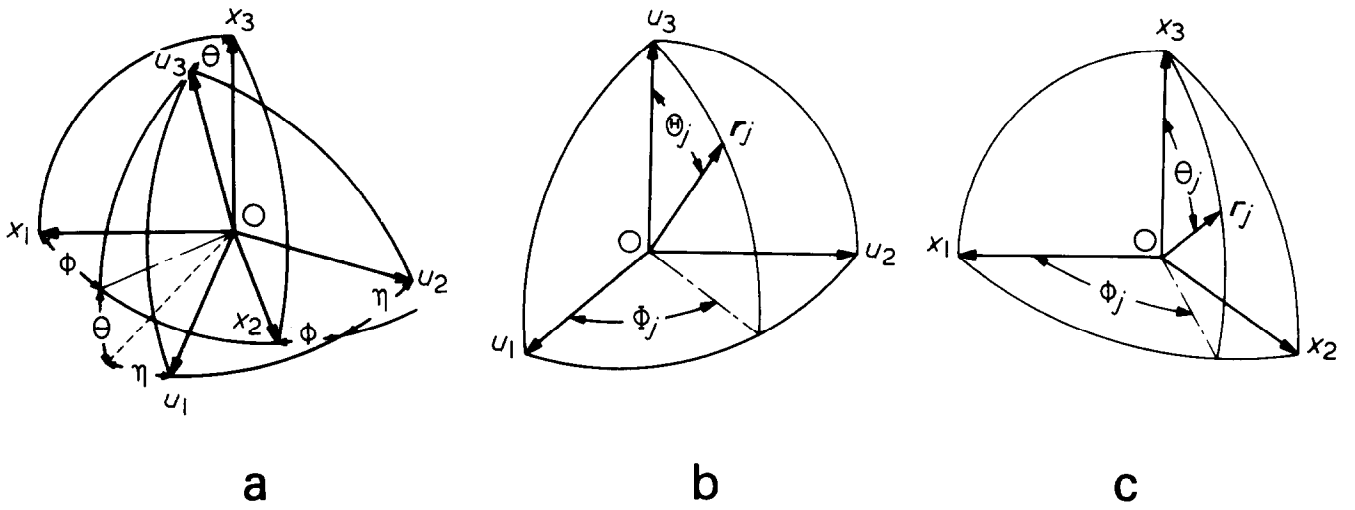


*Figure 2* (a) Three Euler angles, $\phi$, $\theta$ and $\eta$, specifying the orientation of a Cartesian coordinate system O–$u_1u_2u_3$ fixed within a crystallite with respect to another Cartesian coordinate system O–$x_1x_2x_3$ fixed within the bulk specimen. (b) Polar and azimuthal angles, $\Theta_j$ and $\Phi_j$, specifying the orientation of the reciprocal lattice vector $r_j$ of the $j$th crystal plane with respect to the Cartesian coordinate system O–$u_1u_2u_3$. (c) Polar and azimuthal angles, $\theta_j$ and $\phi_j$, specifying the orientation of the $r_j$ vector with respect to the Cartesian coordinate system O–$x_1x_2x_3$

orders of the series expansion, and where $l$ and $n$ are even numbers and $m$ is zero.*

In turn, the coefficients of the expanded series, $A_{l0n}$ and $\alpha^j_{l0}$, can be represented by

$$A_{l0n}=\frac{1}{2\pi}\int_0^{2\pi}\int_{-1}^{1} w(\xi,0,\eta)\Pi^n_l(\xi)\cos(n\eta)\,d\xi\,d\eta \qquad (5)$$

$$\alpha^j_{l0}=\int_{-1}^{1} q_j(\zeta_j,0)\Pi_l(\zeta_j)\,d\zeta_j \qquad (6)$$

As can be recognized from equations (5) and (6), the coefficients are the averages of the distribution functions with respect to the spherical harmonics of the $l0n$-th and $l0$-th orders, respectively. In other words, the coefficients are explicitly the $l0n$-th and $l0$-th moments of the orientation distribution functions, respectively, and are very significant for defining the uniaxial orientation factors, in general, as proposed by Nomura *et al.*[28]

Applying a generalization of the Legendre addition theorem to a relation interrelating the two sets of polar and azimuthal angles, $\Theta_j$ and $\Phi_j$ and $\theta_j$ and $\phi_j$ to each other through the three Euler angles, $\phi$, $\theta$ and $\eta$, the following relation may be obtained:

$$\alpha^j_{l0}=2\pi\left(\frac{2}{2l+1}\right)^{1/2}\left[A_{100}\Pi_l(\cos\Theta_j)+2\sum_{n=2}^{l}A_{l0n}\Pi^n_l(\cos\Theta_j)\cos(n\Phi_j)\right] \qquad (7)$$

Equation (7) is one of the most significant results in the above mathematical structure, interrelating not only the two coefficients, $\alpha^j_{l0}$ and $A_{l0n}$, to each other, but also the coefficients $\alpha^j_{l0}$ of different $j$th planes to each other, as discussed by Sack[29] and Wilchinsky[30], and enabling us to determine the orientation distribution function $w(\xi,0,\eta)$ from the measurable function $q_j(\zeta_j,0)$ and further from $\alpha^j_{l0}$ to an approximation depending upon the possible number of $j$s.

The uniaxial orientation distribution function of the $j$th crystal plane, $q_j(\zeta_j,0)$, can be obtained from the X-ray diffraction intensity distribution at a given twice the Bragg angle of the plane, $I_j(\theta_j,\phi_j=90°)$, as follows:

$$q_j(\zeta_j,0)=I_j(\theta_j,\phi_j=90°)\Big/4\pi\int_0^{\pi/2} I_j(\theta_j,\phi_j=90°)\sin\theta_j\,d\theta_j \qquad (8)$$

Once the $q_j(\zeta_j,0)$ is determined, $\alpha^j_{l0}$ can be calculated from equation (6) for any even numbers of $l$. Using $\alpha^j_{l0}$ thus determined and $\Theta_j$ and $\Phi_j$, which are known for a given $j$th crystal plane, as listed in *Table 1*, the coefficient $A_{l0n}$ can be calculated from equation (7) by solving simultaneous equations of (7) varying $j$ up to at least $(\frac{1}{2}l+1)$. In turn, the orientation distribution function of the crystallites, $w(\xi,0,\eta)$, can be determined from equation (3) with the approximation of finite series of the expansion up to $l=2(j-1)$, instead of the infinite series of the expansion.

When a dynamic mechanical excitation is imposed in a tensile manner upon a bulk specimen with a small enough

* The Cartesian coordinate system, O–$x_1x_2x_3$, must be fixed within the bulk specimen in such a way that the $x_1$-, $x_2$- and $x_3$-axes are parallel to the thickness, transverse and machine directions of the calendered films to give the orientation distribution of the crystallites orthogonal–biaxial symmetry and further uniaxial symmetry with respect to the machine direction. The Cartesian coordinate system, O–$u_1u_2u_3$, must be fixed within the polyethylene crystallite (orthorhombic crystal) to be parallel to its principal crystallographic axes, such that the $u_1$-, $u_2$- and $u_3$-axes are parallel to the $a$-, $b$- and $c$-axes, respectively. The cylindrical symmetry (uniaxial symmetry) of the orientation distribution of the $r_j$ vectors with respect to the machine direction ($x_3$-axis) makes the angular distributions of $\phi$ and $\phi_j$ random, denoted $w(\xi,\phi=0,\eta)$ and $q_j(\zeta_j,\phi_j=0)$ in equations (3) and (4).

amplitude of dynamic strain $\Delta\lambda$ superimposed on a static strain of $\lambda^\circ$, i.e.

$$\lambda(t)=\lambda^\circ+\Delta\lambda\, e^{i\omega t} \tag{9}$$

then the X-ray diffraction intensity distribution $I_j(\theta_j,\phi_j)$ must respond linearly in uniaxial symmetric fashion as[18]:

$$I_j(\theta_j,0,t)=I_j^\circ(\theta_j,0)+\Delta I_j^*(\theta_j,0)e^{i\omega t} \tag{10}$$

where $\Delta I_j^*\,(=\Delta I_j'+i\Delta I_j'')$ is the dynamic complex amplitude of the X-ray diffraction intensity distribution, $\omega$ is angular velocity, and superscript o denotes static component at $\lambda^\circ$.

In analogy with equation (8), one can define the static and dynamic components of $q_j(\theta_j,0,t)$ as follows:[17]

$$q_j^\circ(\theta_j,0)=I_j^\circ(\theta_j,0)\Big/4\pi\int_0^{\pi/2}I_j^\circ(\theta_j,0)\sin\theta_j\,d\theta_j \tag{11}$$

$$\Delta q_j'(\zeta_j,0)=\Delta I_j'(\theta_j,0)\Big/4\pi\int_0^{\pi/2}I_j^\circ(\theta_j,0)\sin\theta_j\,d\theta_j \tag{12}$$

$$\Delta q_j''(\zeta_j,0)=\Delta I_j''(\theta_j,0)\Big/4\pi\int_0^{\pi/2}I_j^\circ(\theta_j,0)\sin\theta_j\,d\theta_j \tag{13}$$

where $\Delta q_j'(\zeta_j,0)$ and $\Delta q_j''(\zeta_j,0)$ are in-phase (real) and out-of-phase (imaginary) components of the complex dynamic orientation distribution function of the $j$th crystal plane with respect to the dynamic bulk strain.

The dynamic response of the expansion coefficient $\alpha_{l0}^j(t)$ can be defined as:

$$\alpha_{l0}^j(t)=\alpha_{l0}^{j0}+(\Delta\alpha_{l0}^{j\prime}+i\Delta\alpha_{l0}^{j\prime\prime})e^{i\omega t} \tag{14}$$

and its static and dynamic components can be further formulated from equation (6) as

$$\alpha_{l0}^{j0}=2\int_0^1 q_j^\circ(\zeta_j,0)\Pi_l(\zeta_j)\,d\zeta_j \tag{15}$$

$$\Delta\alpha_{l0}^{j\prime}=2\int_0^1\Delta q_j'(\zeta_j,0)\Pi_l(\zeta_j)\,d\zeta_j \tag{16}$$

$$\Delta\alpha_{l0}^{j\prime\prime}=2\int_0^1\Delta q_j''(\zeta_j,0)\Pi_l(\zeta_j)\,d\zeta_j \tag{17}$$

Similarly, the dynamic response of the expansion coefficient $A_{l0n}(t)$ can be defined as:

$$A_{l0n}(t)=A_{l0n}^\circ+(\Delta A_{l0n}'+i\Delta A_{l0n}'')e^{i\omega t} \tag{18}$$

and equation (7) must be modified for dynamic response as follows:

$$\alpha_{l0}^{j0}=2\pi\left(\frac{2}{2l+1}\right)^{1/2}\left(A_{l00}^\circ\Pi_l(\cos\Theta_j)+2\sum_{n=2}^{l}A_{l0n}^\circ\Pi_l^n(\cos\Theta_j)\cos(n\Phi_j)\right) \tag{19}$$

$$\Delta\alpha_{l0}^{j\prime}=2\pi\left(\frac{2}{2l+1}\right)^{1/2}\left(\Delta A_{l00}'\Pi_l(\cos\Theta_j)+2\sum_{n=2}^{l}\Delta A_{l0n}'\Pi_l^n(\cos\Theta_j)\cos(n\Phi_j)\right) \tag{20}$$

$$\Delta\alpha_{l0}^{j\prime\prime}=2\pi\left(\frac{2}{2l+1}\right)^{1/2}\left(\Delta A_{l00}''\Pi_l\cos\Theta_j)+2\sum_{n=2}^{l}\Delta A_{l0n}''\Pi_l^n(\cos\Theta_j)\cos(n\Phi_j)\right) \tag{21}$$

Furthermore, the dynamic response of the orientation distribution function of the crystallites $w(\xi,0,\eta,t)$ can be defined as:

$$w(\xi,0,\eta,t)=w^\circ(\xi,0,\eta)+[\Delta w'(\xi,0,\eta)+i\Delta w''(\xi,0,\eta)]e^{i\omega t} \tag{22}$$

where $w^\circ(\xi,0,\eta)$ is the static component at $\lambda=\lambda^\circ$, and $\Delta w'(\xi,0,\eta)$ and $\Delta w''(\xi,0,\eta)$ are in-phase (real) and out-of-phase (imaginary) components of the complex dynamic orientation distribution function of the crystallites, respectively. Each component can be given from equation (3) as follows:

$$w^\circ(\xi,0,\eta)=\sum_{l=0}^{\infty}A_{l00}^\circ\Pi_l(\xi)+2\sum_{l=2}^{\infty}\sum_{n=2}^{l}A_{l0n}^\circ\Pi_l^n(\xi)\cos(n\eta) \tag{23}$$

$$\Delta w'(\xi,0,\eta)=\sum_{l=0}^{\infty}\Delta A_{l00}'\Pi_l(\xi)+2\sum_{l=2}^{\infty}\sum_{n=2}^{l}\Delta A_{l0n}'\Pi_l^n(\xi)\cos(n\eta) \tag{24}$$

$$\Delta w''(\xi,0,\eta)=\sum_{l=0}^{\infty}\Delta A_{l00}''\Pi_l(\xi)+2\sum_{l=2}^{\infty}\sum_{n=2}^{l}\Delta A_{l0n}''\Pi_l^n(\xi)\cos(n\eta) \tag{25}$$

Similarly to the determination of $w(\xi,0,\eta)$ from $q_j(\zeta_j,0)$, as mentioned above, the static and dynamic components, $w^\circ(\xi,0,\eta)$, $\Delta w'(\xi,0,\eta)$ and $\Delta w''(\xi,0,\eta)$ can be determined from $q_j^\circ(\zeta_j,0)$, $\Delta q_j'(\zeta_j,0)$ and $\Delta q_j''(\zeta_j,0)$ through the determinations of $\alpha_{l0}^\circ$, $\Delta\alpha_{l0}'$ and $\Delta\alpha_{l0}''$ and $A_{l0n}^\circ$, $\Delta A_{l0n}'$ and $\Delta A_{l0n}''$, respectively, by use of the respective equations from (14) through (25), all with the approximation of finite series of expansion up to $l=2(j-1)$.

## EXPERIMENTAL RESULTS AND DISCUSSION

### *Morphology of calendered film and crystal orientation behaviour during stretching the film along machine direction*

According to our previous electron microscope (EM) and small-angle X-ray scattering (SAXS) studies[21,22], the above-mentioned calendered specimen possesses a crystalline texture of cylindrites in which stacks of crystal lamellae are oriented radially with their lamellar axes perpendicular to the machine direction of fabrication. These lamellae are thought to overgrow from rows of

nucleating points, as proposed by Keller and Machin[31], to form a sort of lamellar network.

*Figure 3* shows a typical electron micrograph of a surface replica of the specimen, etched by fuming nitric acid at 60°C for 3 h and shadowed by platinum vapour with shadowing angle of 45°. Typically of the film crystallized from oriented melts, the stack of crystal lamellae is seen to be highly oriented with their lamellar axes perpendicular to the machine direction. The high degree of lamellar orientation can also be seen in *Figure 4* in which the appearance of two-point SAXS pattern in the meridional direction for the unstretched specimen and its change with stretching the specimen in the MD are shown. Upon stretching the specimen in the MD, the following changes in the lamellar network may be seen in the figures; (a) increase of interlamellar spacing from 230 Å to 270 and 300 Å with increase of the extension ratio from 1.0 to 1.2 and 1.4, which is associated with shifting the position ($2\theta_{max}$) of the meridional SAXS intensity maximum to a lower scattering angle; (b) an increase of interlamellar void formation or lower density region to some degree as a consequence of process (a), which is to a lesser extent than the case of a row-nucleated high-density polyethylene of *c*-axis orientation[4,5] and is associated with increase of the SAXS intensity especially at angles lower than $2\theta_{max}$; and (c) increasing degree of lamellar bending and irregular deformation of lamellae, which is associated with an increase of lateral breathing of the two-point SAXS patterns. The increase in the SAXS intensity must be related to a negative form birefringence and a whitening of the specimen during stretching in the MD, which are also to a lesser extent, as will be discussed later, than the case of the row-nucleated *c*-axis orientation specimen[32-34].

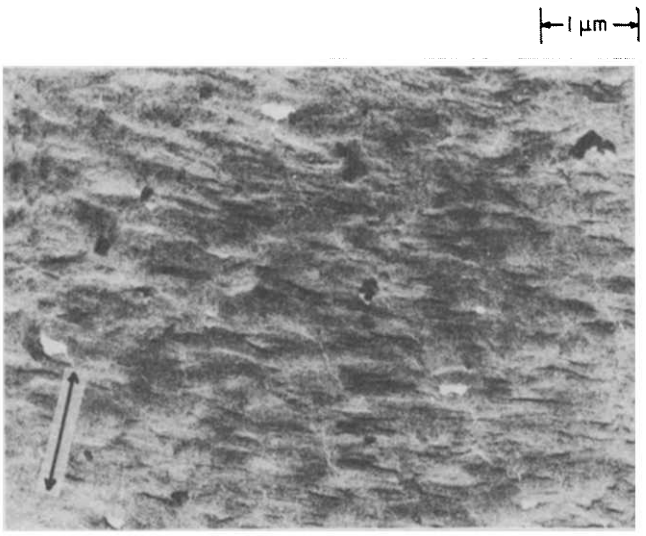


*Figure 3* A typical electron micrograph of a surface replica of the specimen. The arrow indicates the machine direction MD

*Figure 5* shows wide-angle X-ray diffraction (WAXD) pattern of through, edge and end of the unstretched specimen. As can be seen in the figure, the through and edge patterns are identical with each other, both demonstrating a preferential *a*-axis orientation towards the MD, while the end pattern is of the so-called Debye–Scherrer rings with uniform diffraction intensity distribution in circular symmetry with respect to the MD. The above SAXS and WAXD patterns indicate not only that the surface structure in *Figure 3* is representative of the structure in bulk, but also that the structure in bulk is a crystalline texture of highly oriented cylindrites in which the crystalline lamellae grown radially are stacked with their *b*-axes (lamellar axes) perpendicular but their crystal *a*-axes preferentially parallel to the machine direction of fabrication, as schematized in *Figure 6*.

Change in the orientation distribution function of crystallites, $w(\xi,0,\eta)$, with the extension ratio $\lambda$ up to 1.4 is shown in *Figure 7*, in which *7a*, *7b* and *7c* on the left-hand side are the results of fixing the Cartesian coordinates O–$u_1u_2u_3$ within the orthorhombic crystal of polyethylene as $u_1$-, $u_2$- and $u_3$-axes parallel to the crystal *a*-, *b*- and *c*-axes, respectively, while *7d*, *7e* and *7f* on the right-hand side are those fixing the Cartesian coordinates as $u_1$-, $u_2$- and $u_3$-axes parallel to the crystal *c*-, *a*- and *b*-axes, respectively. As can be seen in *Figures 7a* and *7d* for the unstretched specimen, the most populous region in the orientation distribution function appear at $\theta \simeq 55°$ and $\eta = 0°$ and $\theta$

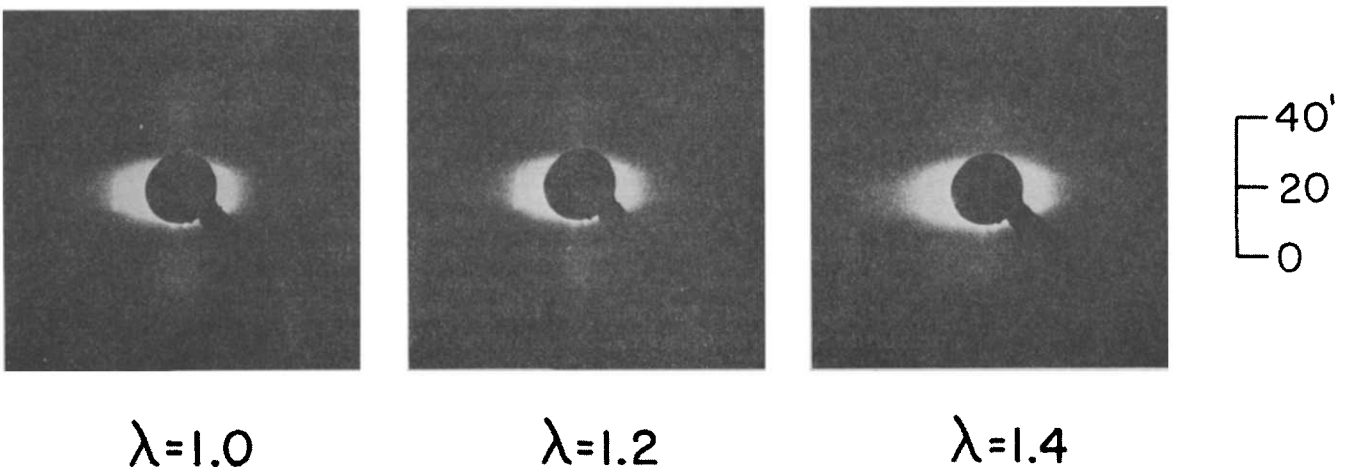


*Figure 4* Change in small-angle X-ray scattering pattern (through radiation) with extension ratio of the specimen in MD. The stretching direction is vertical

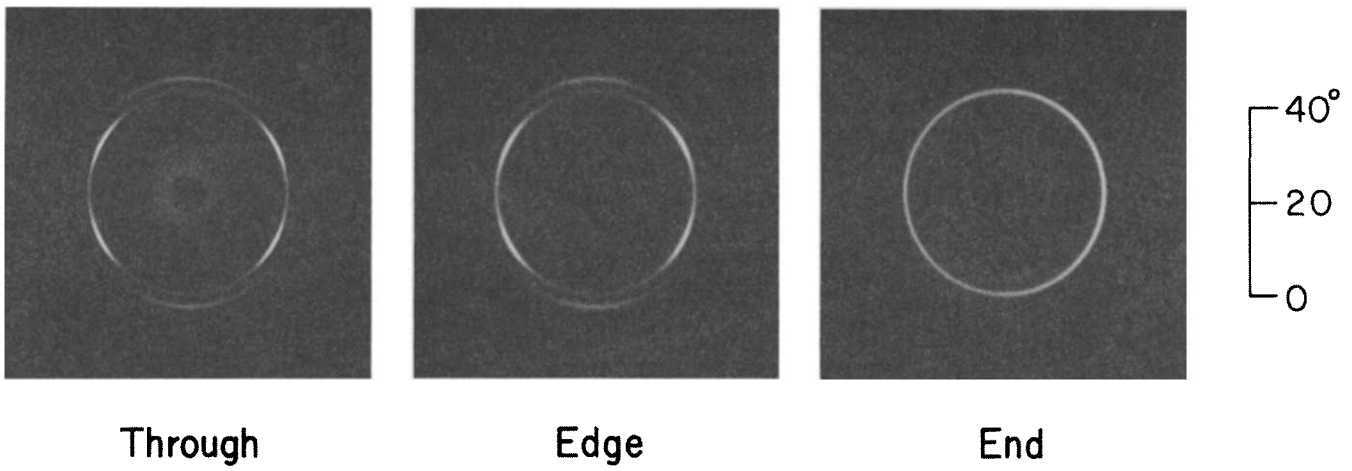


*Figure 5* Wide-angle X-ray diffraction patterns with through, edge and end radiations to unstretched specimen

$=90°$ and $\eta \simeq 55°$, respectively. These results indicate an almost complete planar orientation of the crystal *b*-axes (lamellar axes) parallel to the $x_1x_2$-plane but perpendicular to the $x_3$-axis (machine direction), and preferential orientations of the crystal *a*-axes and *c*-axes towards and away from, respectively, the $x_3$-axis, as suggested in the SAXS and WAXD patterns in *Figures 4* and *5*. The preferential orientations of the crystal *a*- and *c*-axes towards and away from the $x_3$-axis must result from somewhat locally concentrated twisting, rather than regular twisting, of the lamellae about their own lamellar axes.

With increase of the extension ratio up to 1.2, the most populous regions move to lower angles of $\theta$ and $\eta$, as can be seen in *Figures 7b* and *7e*, i.e. to the regions of $\theta \simeq 35°$ and $\eta = 0°$ and $\theta = 90°$ and $\eta \simeq 35°$, respectively, accompanied by broadening of the intensity distribution to the ranges of higher angles of $\theta$ and $\eta$ and lower angles of $\theta$ and $\eta$, respectively, than those in *Figures 7a* and *7d*. This behaviour must be interpreted in terms of a combination of lamellar detwisting with lamellar bending. That is, the lamellar detwisting about the lamellar axis (or rotation of crystal grains within the lamella about their own crystal *b*-axes) to orient the surface normal of lamellar segments (or crystal *c*-axes) towards the $x_3$-axis and the lamellar

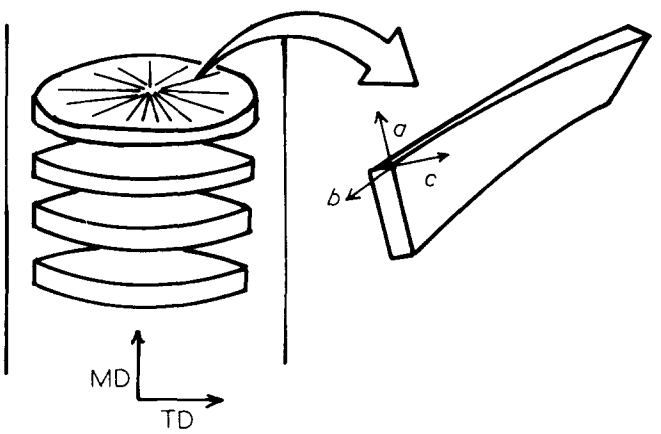


*Figure 6* Schematic diagram illustrating the crystalline morphology of the specimen with preferential *a*-axis orientation

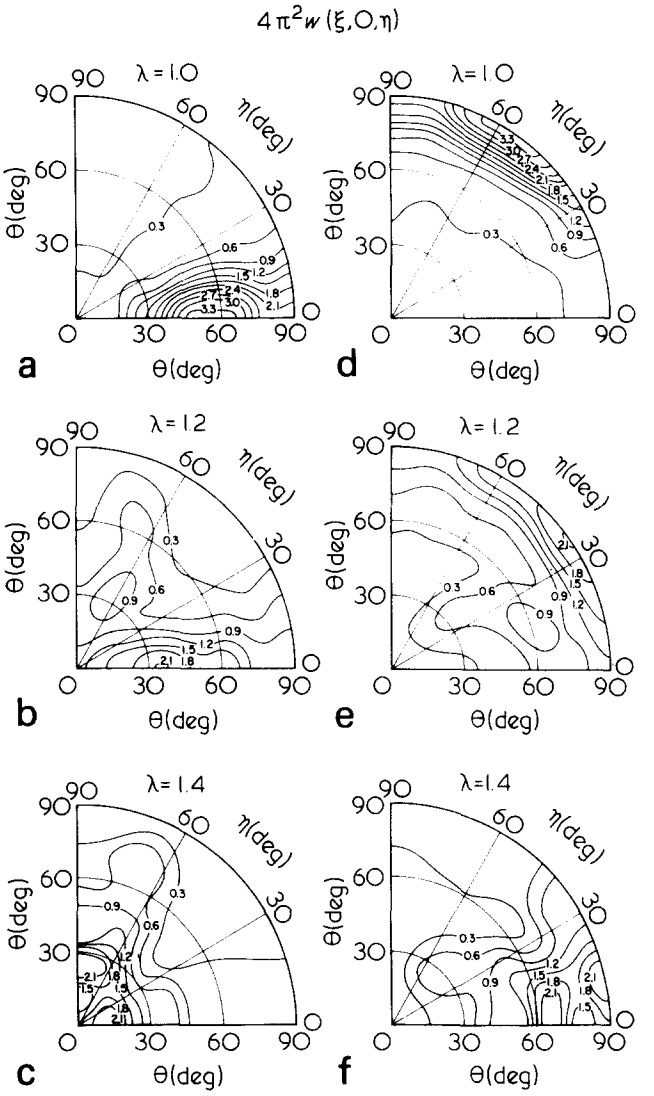


*Figure 7* Change in orientation distribution function of crystallites, $w(\xi, 0, \eta)$, of the specimen with extension ratio $\lambda$ up to 1.4 along the MD. In (a)–(c) the coordinate system O–$u_1u_2u_3$ is fixed within the polyethylene crystal as $u_1$, $u_2$ and $u_3$ parallel to the crystal *a*-, *b*- and *c*-axes, while in (d)–(f) the coordinate system is fixed as $u_1$, $u_2$ and $u_3$ parallel to the crystal *c*-, *a*- and *b*-axes, respectively

bending to orient the lamellar axes also towards the $x_3$-axis.

With further increase of the extension ratio up to 1.4, the most populous regions move further to lower angles of $\theta$ and $\eta$, as can be seen in *Figures 7c* and *7f*, respectively, and result in two subpopulous regions: (a) populous regions at $\theta \simeq 10°$ and $\eta = 0°$ and $\theta = 90°$ and $\eta \simeq 10°$ and (b) populous regions at $\theta \simeq 20°$ and $\eta = 90°$ and $\theta \simeq 70°$ and $\eta = 0°$. The populous regions (a) must result from further progress of the lamellar detwisting, while the development of the populous regions (b) must be interpreted in terms of further progress of the lamellar bending associated with more irregular deformation of the lamellae, such as lamellar tilting to rotate the lamellar segments (or the crystal grains within the lamellae) about their own crystal axes, again so as to orient the crystal $c$-axes towards the $x_3$-axis. As discussed fully in a previous paper[17], a spherulite deformation model combining orientation of the crystal lamellar in affine fashion with a particular reorientation of the crystal grains within the lamellae, such as preferential $c$-axis orientation associated with rotation of the crystal grains about their own $a$-axes, gives rise to the populous regions at $\eta$ of 90° and 0° in $w(\xi,0,\eta)$, as in *Figures 7c* and *7f*, respectively.

*Figure 8* shows the tensile stress–strain behaviour of the present specimen along the MD and TD (thick lines) in comparison with those of a previous specimen of row-nucleated high-density polyethylene of $c$-axis orientation (thin lines)[4], both at a room temperature of 25°C with a strain rate of 100% $min^{-1}$. As can be seen in the figure, the behaviour along the TD shows a discrete yielding phenomenon at several per cent elongation for both specimens, which is followed by a plastic deformation associated with macroscopic necking and large breaking elongation up to several hundred per cent. On the other hand, the behaviour along the MD is much stiffer than that along the TD for both specimens, exhibiting no discrete yielding phenomenon but whitening of the bulk specimen more or less at a few tens of per cent elongation, followed by no trace of macroscopic necking but a rather small breaking elongation up to several tens of per cent.

When the behaviour along the MD of the two specimens is compared, the behaviour of the present specimen of $a$-axis orientation is much less stiff than that of the previous specimen of $c$-axis orientation. The tensile deformation mechanism of the specimens along the MD must involve lamellar detwisting, bending and possibly tilting, as mentioned above. The allowance for lamellar detwisting (rotation of the lamellar segments or crystal grains about the lamellar axis or crystal $b$-axes) must be less for the previous specimen of preferential $c$-axis orientation than for the present specimen of preferential $a$-axis orientation, requiring much more bending of the lamellae at an earlier stage of elongation and stiffening the tensile behaviour of the specimen. Actually, the previous specimen becomes much more whitened than the present specimen and exhibits the so-called hard elasticity.

### *Dynamic mechanical dispersion*

*Figures 9* and *10* show the temperature dependences of the storage and loss compliance functions of the MD and TD specimens, respectively, over temperatures ranging from 10° to 100°C. The storage compliance functions for both specimens increase with increasing temperature or decreasing frequency, whereas the loss compliance functions show a somewhat broad dispersion peak at elevated temperatures for both specimens. The rapid increases in the storage compliance as well as in the maximum value of the loss compliance at the dispersion peak with ascending temperature imply that a conventional frequency–temperature superposition simply by a horizontal shift along the logarithmic frequency axis is not

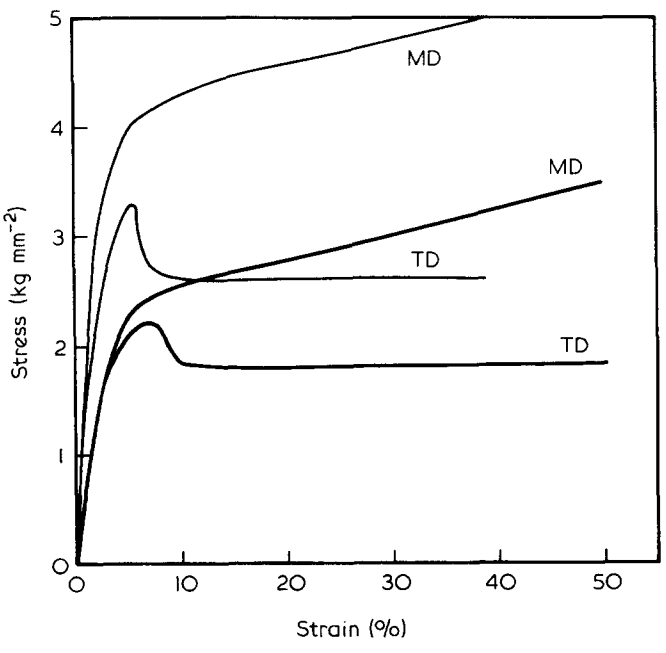


*Figure 8* Tensile stress–strain behaviour of the present specimen along the MD and TD (thick lines) in comparison with those of a previous specimen of row-nucleated high-density polyethylene of $c$-axis orientation (thin lines)

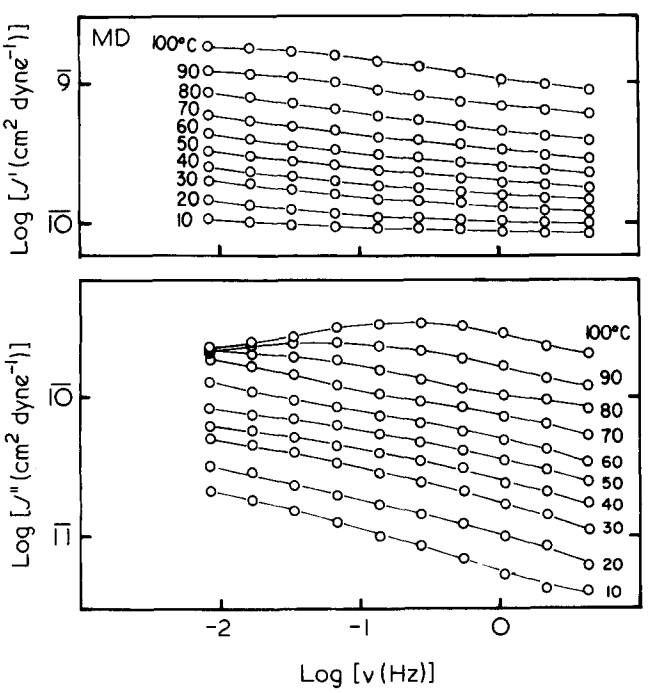


*Figure 9* Temperature dependences of the storage and loss compliance functions, $J'(\omega)$ and $J''(\omega)$, of the MD specimen

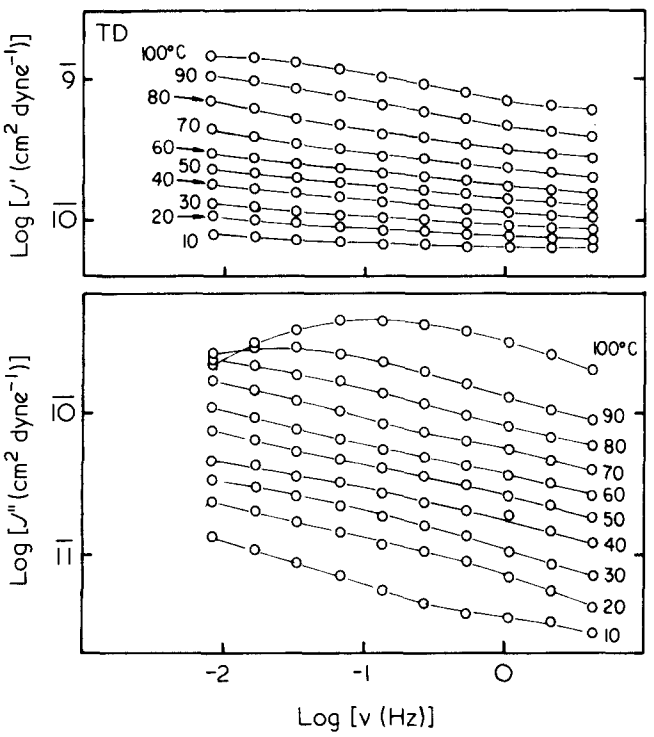


*Figure 10* Temperature dependences of the storage and loss compliance functions, $J'(\omega)$ and $J''(\omega)$, of the TD specimen

likely to be valid, leading to the requirement of a vertical shift in combination with a horizontal shift to obtain a good superimposed master curve. Such a superposition is usually arbitrary and thus an attempt has been made to minimize the uncertainty of the procedure by shifting the storage and loss compliance functions simultaneously so that the best-fit shift factors can be determined.

Apparent superimposed master curves of the storage and loss compliance functions, without taking into account the coexistence of any different retardation mechanisms and being reduced to a common reference temperature of 50°C, are shown in *Figures 11* and *12* for the MD and TD specimens, respectively. As can be seen

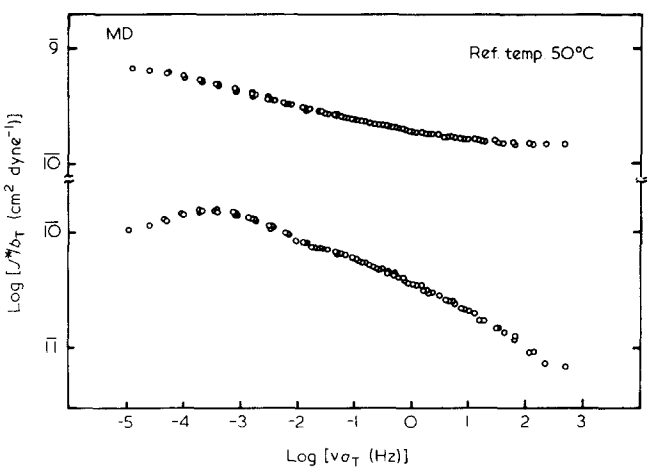


*Figure 11* Apparent master curves of the storage and loss compliance functions of the MD specimen, reduced to a reference temperature of 50°C

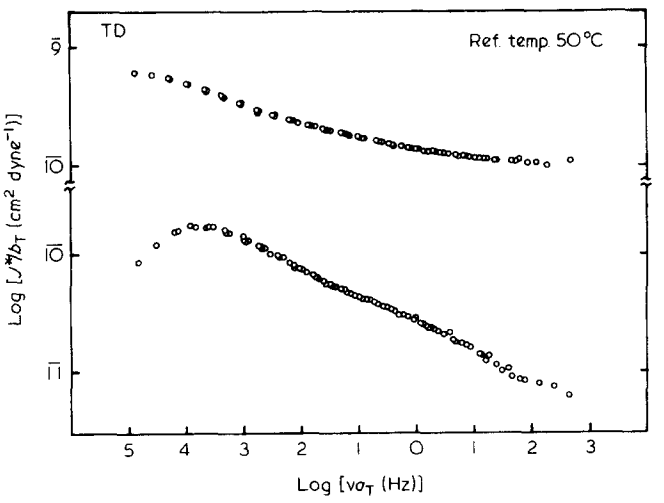


*Figure 12* Apparent master curves of the storage and loss compliance functions of the TD specimen, reduced to a reference temperature of 50°C

from the figures, the frequency dispersion, though corresponding to the $\alpha$ mechanical dispersion of polyethylene, is very vast for both specimens in that it is characterized by a very broad and asymmetric peak of the loss compliance master curve. Such a broad dispersion may be expected for a system composed of more than a single retardation mechanism. It is noteworthy that the apparent frequency dispersion is a little more vast for the MD specimen than for the TD specimen, revealing a somewhat discrete shoulder in the loss compliance function at −1.5 in the logarithmic reduced frequency.

The activation energies, estimated from the Arrhenius plot of the horizontal shift factor vs reciprocal of the absolute temperature, are found, as shown in the upper half of *Figure 13*, to be 21.4 and 34.8 kcal $mol^{-1}$ for the MD specimen and 21.2 and 35.0 kcal $mol^{-1}$ for the TD specimen. These values are in good accord with the reported literature values for the so-called $\alpha_1$ and $\alpha_2$ dispersion processes of high-density polyethylene[8,32,33]. The vertical shift factors required for superimposing the apparent master curves in *Figures 11* and *12* for the MD and TD specimens are plotted against temperature in the lower half of *Figure 13*. Within experimental error, the vertical shift factors for the two specimens are in good agreement, and are comparable with those obtained for the previous specimen of *c*-axis orientation[7] as well as for the low- and medium-density spherulitic polyethylenes[1].

*Dynamic optical dispersion*

The dynamic birefringence results obtained simultaneously with the mechanical data are analysed in terms of real and imaginary components of the complex dynamic stress–optical coefficient function, i.e.

$$\left.\frac{\partial \Delta n^*}{\partial \sigma^*}\right|_{\sigma=\sigma^0} = M^*(=M'-iM'')$$

*Figure 14* shows the temperature dependence of the real and imaginary components, $M'$ and $M''$, for the MD specimen over temperatures ranging from 10° to 100°C. The real component $M'$ at low temperatures remains at slightly but definitely negative values. With ascending temperature, the $M'$ curves turn towards zero and even-

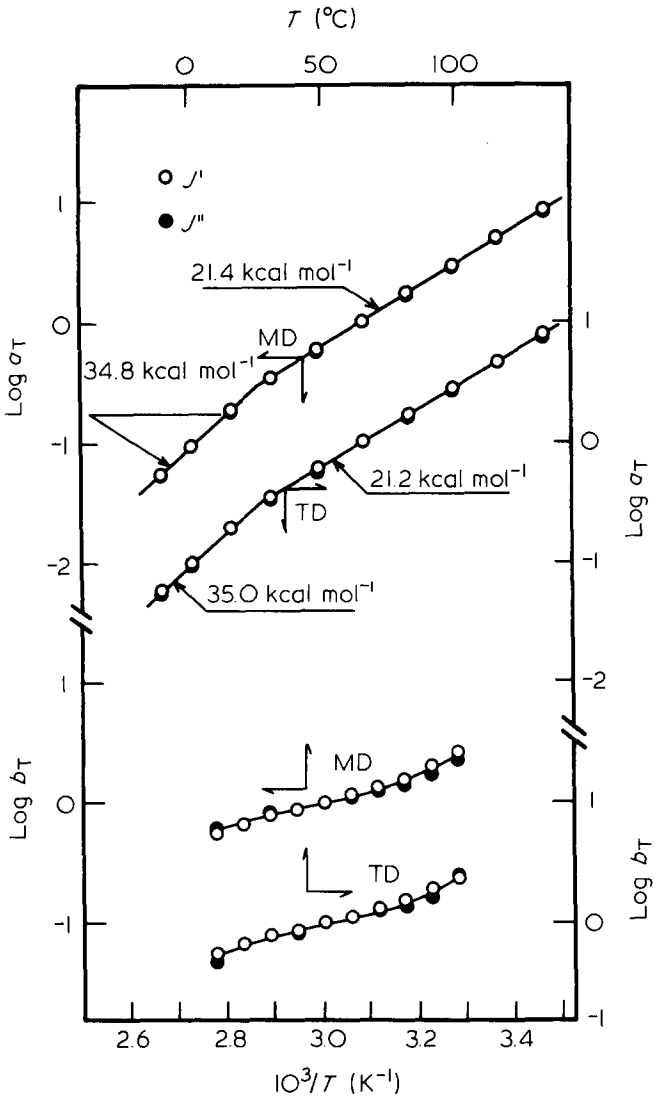


*Figure 13* Temperature dependences of the horizontal and vertical shift factors, $a_T$ and $b_T$, to compose the apparent master curves

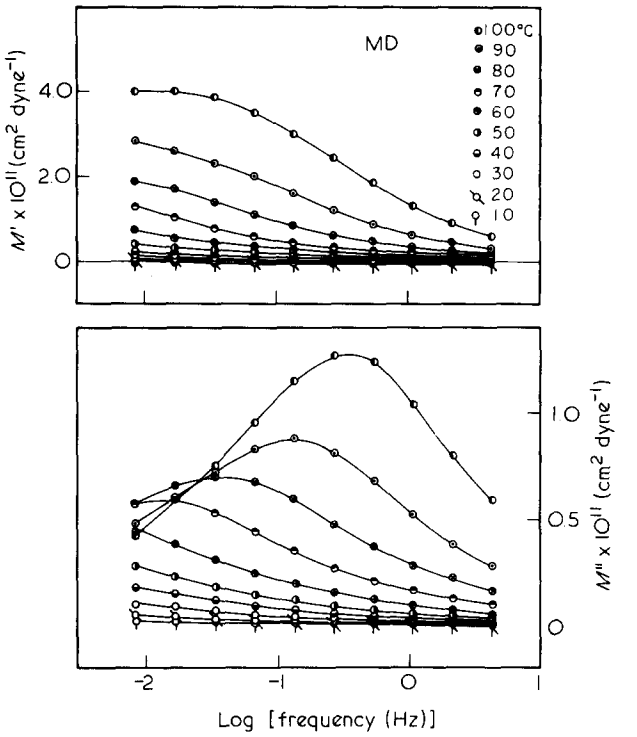


*Figure 14* Temperature dependences of the real and imaginary components of the complex dynamic stress–optical coefficient function, $M'(\omega)$ and $M''(\omega)$, of the MD specimen

tually change to positive values. Around 100°C, the $M'$ curve tends to reach a limiting value of about $4.0 \times 10^{11}$ cm$^2$ dyne$^{-1}$ and levels off. The negative $M'$, though being slight, may be explained as arising from a negative form birefringence associated with the lamellar bending process, as will be discussed later, whereas the positive $M'$ must be attributed to the lamellar detwisting process involving dynamic rotation of the crystal *a*- and *c*-axes around the crystal *b*-axis in such a way that the crystal *c*-axis aligns towards the stretching direction. It is interesting to note that the negative $M'$ is far less in magnitude than that for the previous specimen of *c*-axis orientation, attaining $-0.2 \times 10^{11}$ cm$^2$ dyne$^{-1}$, whereas the positive $M'$ is much greater in its limiting value than that for the previous specimen, reaching $1 \times 10^{11}$ cm$^2$ dyne$^{-1}$. These contrasts in the optical behaviour are consistent with those in the tensile stress–strain behaviour of the two specimens along the MD, as mentioned above, and must be attributed to the difference in the contributions of the two types of deformation mechanisms, i.e. much easier in the lamellar detwisting process but rather hard in the lamellar bending process for the present specimen than for the previous specimen.

The imaginary component $M''$ increases with decreasing frequency, but shows frequency dispersion peaks at elevated temperatures. As can be seen from the figure, the magnitude of the maximum peak, which is also much larger than that for the previous specimen, attaining $0.5 \times 10^{11}$ cm$^2$ dyne$^{-1}$, increases with ascending temperature. These suggest that a conventional frequency–temperature superposition by simply shifting the data along the logarithmic frequency axis is invalid, leading to the requirement of a vertical shift as well as a horizontal shift in the superposition procedure. The same sign of $M'$ and $M''$ at relatively high temperatures implies that the orientational birefringence associated with the lamellar detwisting process lags behind the bulk stress. However, the difference in sign of $M'$ and $M''$ at low temperatures or high frequencies should not necessarily mean that the negative form birefringence leads the bulk stress, because the birefringence dispersion is not only caused by the lamellar bending but also by the lamellar detwisting process. Unless the contribution of each process to the birefringence dispersion is separated quantitatively, no conventional interpretation of the phase relation is applicable.

The complementary results of the $M'$ and $M''$ of the TD specimen are illustrated in *Figure 15*. Contrary to the $M'$ of the MD specimen in *Figure 14*, the $M'$ has positive values even at low temperatures which increase steadily with decreasing frequency. The increase of $M'$ with decreasing frequency becomes more rapid at elevated temperatures. The $M''$ also increases with decreasing frequency at low temperatures but shows a dispersion peak at elevated temperatures. The optical behaviour of the present specimen is quite similar to that of the

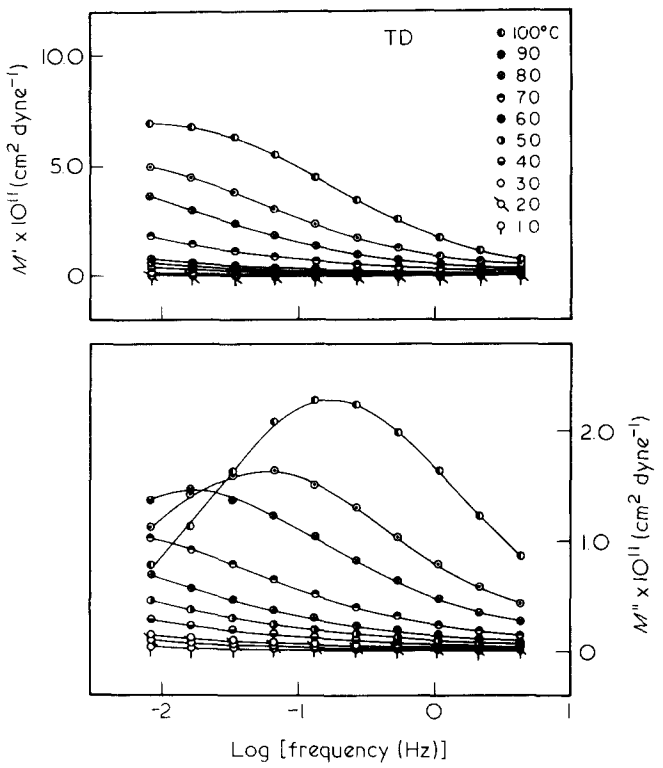


*Figure 15* Temperature dependences of the real and imaginary components of the complex dynamic stress–optical coefficient function, $M'(\omega)$ and $M''(\omega)$, of the TD specimen

previous specimen of *c*-axis orientation, with the exception of somewhat larger magnitudes of $M'$ and $M''$ for the present specimen than for the previous specimen, and the deformation process responsible for the optical dispersion must be explained from a dynamic X-ray diffraction study for the previous specimen[4] in terms of the intralamellar shearing involving the rotation of the lamellar segments or the crystal grains within the lamellae, i.e. the rotation of the crystal *b*- and *c*-axes about the crystal *a*-axis to orient the crystal *c*-axis towards the stretching direction. The same sign of $M'$ and $M''$ indicates that the orientational birefringence associated with the intralamellar shearing lags behind the bulk stress. It should be pointed out that the magnitudes of $M'$ as well as of $M''$ are larger in the TD specimen than in the MD specimen, possibly due to no contribution of the negative form birefringence to the behaviour of the TD specimen.

A conventional frequency–temperature superposition with a simple horizontal shift along the logarithmic frequency axis no longer seems valid for the $M^*$ of the TD specimen as well as the MD specimen. Contrary to the storage and loss compliance functions, the $M^*$ are not sustained either at positive or negative values, changing from positive to negative or vice versa depending upon the intrinsic birefringence of the responding constituent units. Thus, the $M^*$ must be plotted on a semilogarithmic scale against frequency. The vertical shift in additive form would lead to resulting vertical shift factors having the same dimension with the $M^*$ which will certainly produce complications and is not desirable as pointed out in a previous paper[1]. Thus, an alternative method for the superposition of such a system is performed by dividing the $M^*$ with a correction factor $q_T$ in such a way that the corrected stress–optical coefficient $M^*/q_T$ may be superimposed by a simple horizontal shift along the logarithmic frequency. The physical meaning of the correction factor $q_T$ will resemble the vertical shift factor $b_T$ in mechanical data. The superimposed master curves of $M^*$ for both MD and TD specimens, reduced to a reference temperature of 50°C, are shown in the upper and lower halves of *Figure 16*, respectively.

The real component of the superimposed master curve $M'/q_T$ of the MD specimen is negative at high reduced frequencies. The imaginary component $M''/q_T$ of the MD specimen exhibits a distinct frequency dispersion peak at a reduced frequency of –2.7 in logarithmic scale at which the $M'/q_T$ shows an inflection. The dispersion peak of the imaginary component is almost symmetric in shape and is sharper than that of the apparent loss compliance peak in *Figure 11*. In *Figure 17*, Arrhenius plots of the horizontal shift factor vs the reciprocal of the absolute temperature can be represented by a single straight line whose activation energy is estimated to be 24.4 kcal $mol^{-1}$, which is in good agreement with that of the $\alpha_1$ mechanical retardation process. This suggests that the lamellar detwisting process dominates in the optical dispersion of the MD specimen.

The $M'/q_T$ of the TD specimen was found to be almost zero, in contrast to the negative value of the MD specimen, at high reduced frequencies, but increases greatly with decreasing frequency. The $M''/q_T$ also shows a distinct dispersion peak at a reduced frequency of –3.1 in logarithmic scale, which is considerably lower than that of the MD specimen, suggesting that the retardation time of the optical dispersion is longer in the TD specimen than in the MD specimen. The activation energy as estimated on the basis of the Arrhenius theory was, however, found to be 25.0 kcal $mol^{-1}$, which is comparable to that obtained for the MD specimen as well as to the literature values for the $\alpha_1$ mechanical dispersion. These facts suggest that only one retardation process, i.e. the intralamellar crystal rotation process, is accentuated in the birefringence dispersion. It is noteworthy that the activation energies required to bring about the crystal orientation dispersions of the rotation of the crystal *a*- and *c*-axes about the *b*-axis dominating in the MD, and the rotation of the crystal *b*-

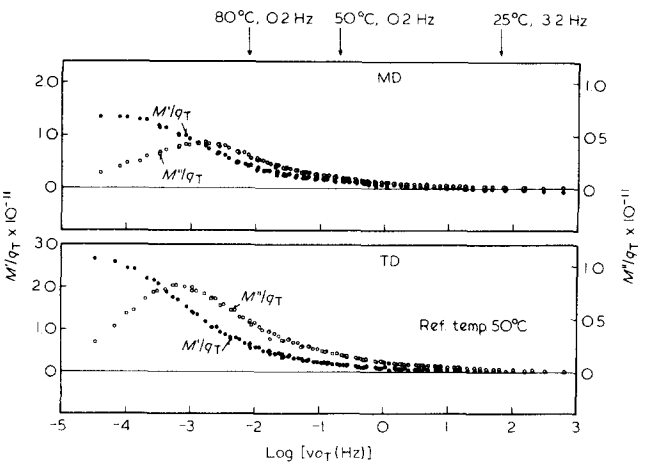


*Figure 16* Master curves of the real and imaginary components of the complex dynamic stress–optical coefficient functions of the MD (upper) and TD (lower) specimens, all reduced to a reference temperature of 50°C

and *c*-axes about the *a*-axis dominating in the TD, are almost the same.

Although the orientational birefringence may not be sensitive to the onset of rotational vibrations of the chain molecules within the crystal lattice, the intrinsic birefringence of the crystal lattice can be influenced by the internal field effect. The reason why no prominent birefringence dispersion corresponding to the $\alpha_2$ mechanical dispersion is observed in the Arrhenius plots of the horizontal shift factor vs $1/T$is that the internal field effect upon the intrinsic birefringence is comparatively smaller than the orientational birefringence at these temperatures or is perhaps diminished in the correction procedure that required a sizeable amount of $q_T$. The $q_T$ required for the superposition is plotted against temperature in *Figure 18* in which $q_T$ changes rather rapidly with temperature. The origin of the temperature dependence of $q_T$ is unclear owing to further complication of the combined influences of the temperature dependences of the intrinsic elastic compliance and birefringence of the corresponding unit. It is felt that the $q_T$ may be related partly to the temperature dependence of the birefringence resulting from the internal field effect and/or crystal disordering effect, whose detail will be discussed elsewhere[34].

*Dynamic orientation distribution function*

In *Figure 19* are shown the real components of the complex dynamic orientation distribution function of the crystallites, $\Delta w'(\xi,0,\eta)$, for the MD specimen at three particular temperatures and frequencies. The Cartesian coordinate system O–$u_1u_2u_3$ was fixed within the polyethylene crystal with $u_1$, $u_2$ and $u_3$ parallel to the crystal *a*-, *b*- and *c*-axes, respectively, so that the results cor-

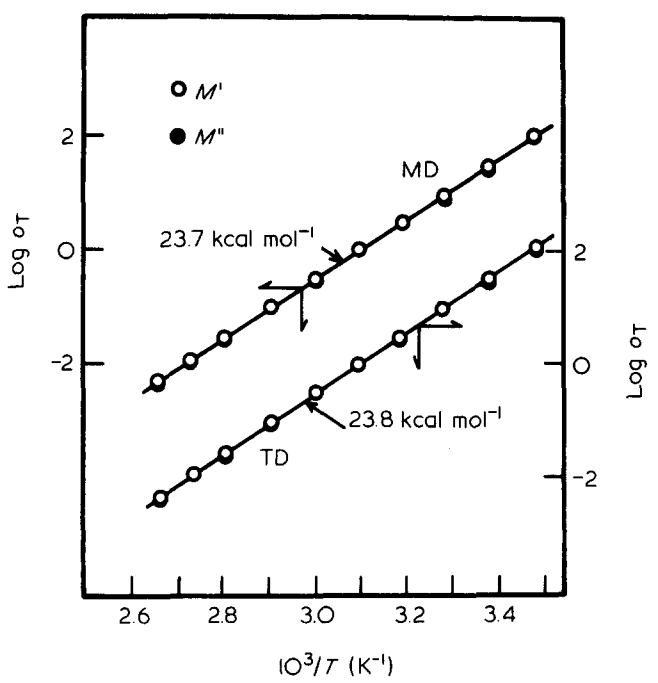


*Figure 17* Arrhenius plots of the horizontal shift factor $a_T$ for composing the master curves of the complex dynamic stress–optical coefficient functions for the MD and TD specimens

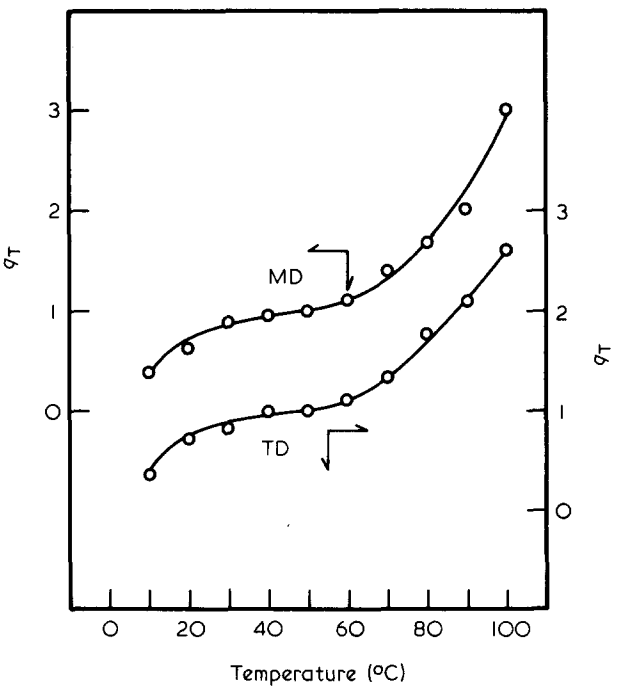


*Figure 18* Temperature dependences of the correction factor (vertical shift factor) $q_T$ for composing the master curves of the complex dynamic stress–optical coefficient functions for the MD and TD specimens

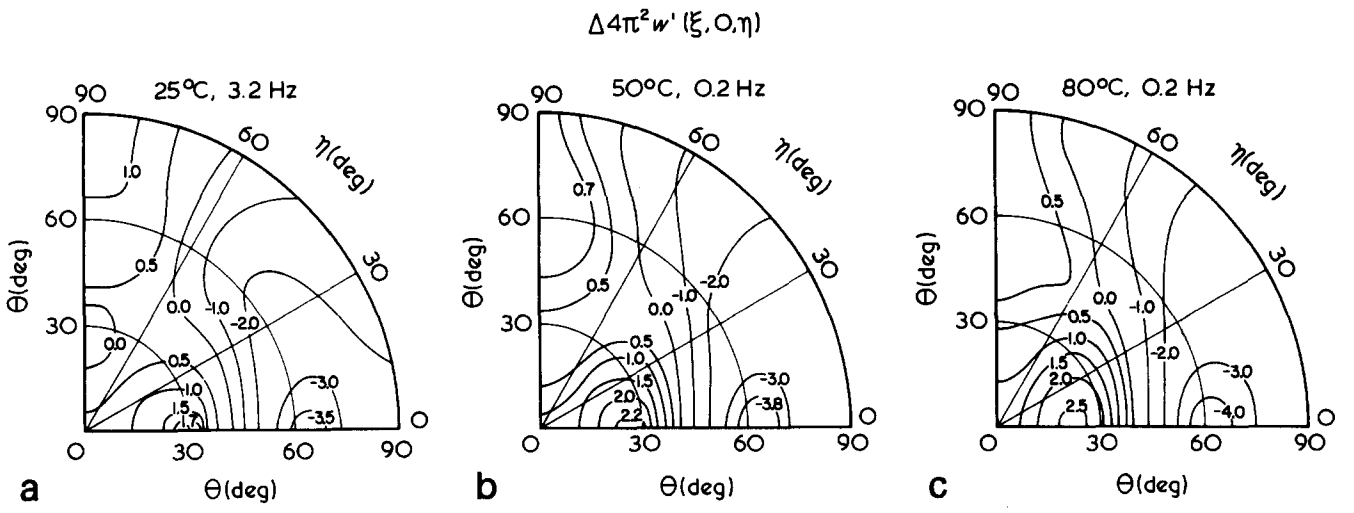


*Figure 19* Real components of the complex dynamic orientation distribution function of the crystallites, $\Delta w'$ ($\xi$, 0, $\eta$), for the MD specimen at different temperatures and frequencies

respond to those on the left-hand side of *Figure 7*. The function was calculated from $\Delta A'_{0n}$ by use of equation (24) with the finite series of expansion up to the 10th order, where the contour line is multiplied in its intensity by a factor of 10 relative to that in *Figure 7*, and the positive or negative sign of the contour line means the increase or decrease in the orientation distribution function relative to that of the static component, $w^o(\xi,0,\eta)$ at $\lambda^o = 1.03$, which must be very similar to *Figure 7a* rather than *Figure 7b*. A similar investigation was carried out to determine the imaginary component of the complex dynamic orientation distribution function of the crystallites, $\Delta w''(\xi,0,\eta)$. The dynamic X-ray diffraction intensity was, however, too weak in its imaginary component to resolve the component into $\Delta I''_j(\theta_j,0)$s for the respective $j$th crystal planes and finally to determine $\Delta w''(\xi,0,\eta)$ through the mathematical procedure mentioned above.

The following characteristics must be noticed in *Figure 19* as temperature increases or frequency decreases: that is, at relatively low temperature of 25°C two populous regions (region A and region B) appear at $\eta \simeq 90°$ and $\theta \simeq 90°$ and at $\eta \simeq 0°$ and $\theta \simeq 30°$, respectively, in association with the losses in the intensity distribution at rather a vast region, but concentrated in a region (region C) at $\eta \simeq 0$ and $\theta \simeq 60°$; and with increasing temperature or decreasing frequency the region A becomes less intensive and flattened while the region B becomes a little more intensive and shifted to smaller angles of $\theta$. When compared with the static component of $w^o(\xi,0,\eta)$, which must resemble $w(\xi,0,\eta)$ in *Figure 7a*, the development of the region B in compensation of the region C can be interpreted in terms of enhancement of the dynamic lamellar detwisting process to orient the crystal $c$-axes to further small angles of $\theta$. The higher the temperature or the lower the frequency, this type of dynamic lamellar detwisting process must be accentuated to intensify and shift the region B to small angles of $\theta$.

As has been discussed fully in a previous paper[17], the development of region A can be interpreted in terms of a progress of preferential $b$-axis orientation of the crystallites towards the stretching direction in association with random rotation of the crystallites about their own $b$-axes, i.e. the lamellar orientation arising from the lamellar bending process. Therefore, the above characteristic behaviour in $\Delta w'(\xi,0,\eta)$ with increase of temperature or decrease of frequency can be explained in terms of the enhancement of the lamellar detwisting process in counterbalance of the lamellar bending process. Although the phase relations in dynamic response of these lamellar detwisting and bending processes with respect to the bulk strain and, consequently, to the bulk stress, are not certain because of the lack of data of $\Delta w''(\xi,0,\eta)$, corresponding reduced frequencies of the three particular temperatures and frequencies at which the measurements were carried out are indicated by three arrows in the upper half of *Figure 16* to assure the discussion postulated for the assignments of the optical dispersion of the MD specimen.

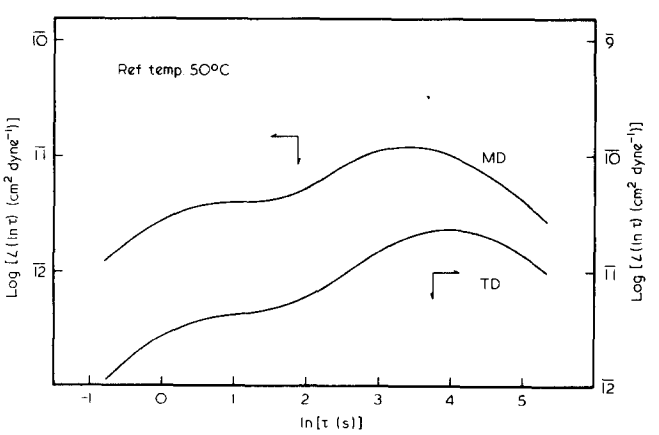


*Figure 20* Mechanical retardation time spectra, $L(\ln \tau)$, at 50°C for the MD and TD specimens

*Mechanical and optical retardation spectra*

*Figure 20* shows the mechanical retardation time spectra of the MD and TD specimens at 50°C, which are determined by a deconvolution method[7] from the apparent master curves of the loss compliance functions in *Figures 11* and *12*. As can be seen in the figure, the spectra could be understood as a superposition of two symmetric distribution functions with respect to logarithmic retardation time, i.e. one at longer retardation time with larger intensity than the other at shorter retardation time. The former must correspond to the $\alpha_2$ retardation process, while the latter to the $\alpha_1$ process. Comparing the spectra between the specimens, the $\alpha_1$ process is almost the same in the intensity distribution of the spectrum, while the $\alpha_2$ process is much more intensive and shifted to longer retardation times in the spectrum for the TD specimen than for the MD specimen.

In order to compare the optical dispersion processes of the MD and TD specimens, the optical retardation time spectra* are computed from the superimposed master curves of the imaginary components $M''$ in *Figure 16* in accordance with the deconvolution method and are shown in *Figure 21*. One can envisage that the retardation spectrum for the TD specimen can be characterized by a little sharper distribution with a slightly larger intensity and longer retardation times than that for the MD specimen, resulting in rather less retardation intensity (the integrated area under the spectral curve) for the MD specimen than for the TD specimen. This suggests that the lamellar detwisting process dominating in the MD specimen is less conspicuous in the optical dispersion than the intralamellar shearing process which dominates in the TD specimen. Judging from the activation energies of the birefringence dispersion for both specimens, which are comparable with that of the $\alpha_1$ mechanical dispersion, it is likely that the orientation dispersion process may primarily be responsible for the $\alpha_1$ process rather than the $\alpha_2$ process. However, the peak positions of these biref-

* The optical retardation time spectrum, $M(\ln \tau)$ can be defined as follows[6]:

$$M'(\omega) = M'(\infty) + \int_{-\infty}^{\infty} \frac{M(\ln \tau)}{1+\omega^2\tau^2} d\ln\tau \tag{26}$$

$$M''(\omega) = \int_{-\infty}^{\infty} \frac{M(\ln \tau)\omega\tau}{1+\omega^2\tau^2} d\ln\tau \tag{27}$$

with normalization

$$\int_{-\infty}^{\infty} \frac{M(\ln \tau)}{M'(0)-M'(\infty)} d\ln\tau = 1 \tag{28}$$

where $\tau$ is the optical retardation time.

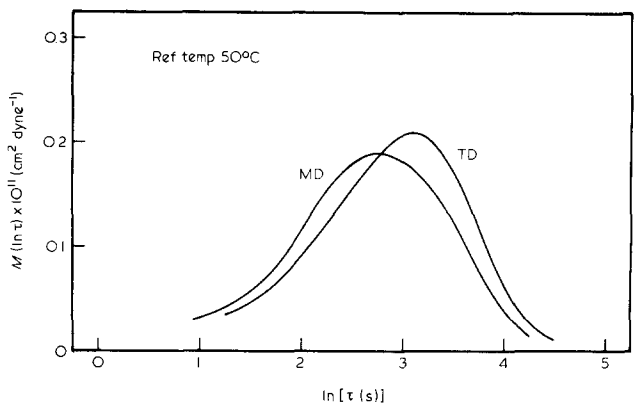


*Figure 21* Optical retardation time spectra, $M(\ln \tau)$, at 50°C for the MD and TD specimens

ringence spectra on the retardation time scale do not correspond to those of the $\alpha_1$ mechanical dispersion. This implies that the orientation dispersion of the crystals occurs in the vicinities of the $\alpha_1$ as well as the $\alpha_2$ mechanical dispersions.

The real and imaginary components of the stress–optical coefficient functions are recomputed from their respective spectra in *Figure 21* for the MD and TD specimens and compared with the observed master curves in *Figure 22*. As can be seen in the figure, the calculated $M''$ agrees well, within the experimental error, with the observed $M''/q_T$ for both specimens, indicating the good accuracy of the deconvolution method at least for the imaginary component, which always gives a positive value even at high reduced frequencies. On the other hand, the calculated curves of $M'-M'(\infty)$ have much greater values than the observed ones at lower reduced frequencies, decrease rapidly with increasing fequency, and converge to zero at highest reduced frequencies for both specimens, giving negative residues after subtracting the calculated values from the observed ones, as indicated by dash–dot lines in the figure, at lower frequencies for the TD specimen but throughout the range of reduced frequency for the MD specimen.

The discrepancy between the calculated and observed $M'$, resulting in certain amounts of the negative residues for both specimens at lower reduced frequencies, may be due partly to the uncertainty of the vertical shift factor $q_T$ at higher temperatures or to the computational error involving the deconvolution procedure to evaluate the spectrum which usually necessitates that the ends of the imaginary component $M''$, approach zero for the convergence of integration during the Fourier transformation. Nevertheless, the negative residue throughout the range of reduced frequency for the MD specimen must be understood as a consequence of an additional negative residue of relatively small but almost constant value irrespective of the reduced frequencies covered. This additional negative residue must be ascribed to the negative form birefringence arising from the lamellar bending process. In contrast, the calculated and observed $M''$ converge to zero at higher reduced frequencies, indicating no trace of negative contribution to the imaginary component. These facts suggest that the lamellar bending process occurs quite in phase with the bulk stress at least in the range of reduced frequency covered, and that the $\alpha$ optical dispersion and possibly the $\alpha$ mechanical dispersion are mostly attributed to the crystal orientation dispersion involving intralamellar shearing processes, i.e. the detwisting and tilting processes of the lamellar segments or the crystal grains within the lamellae for the MD and TD specimens, respectively. The optical dispersion associated with the lamellar bending process, if any, may be expected at higher frequencies and lower temperatures than those covered here to assign the $\beta$ mechanical dispersion to the interlamellar shearing process.

## CONCLUSION

Tensile dynamic deformation mechanism of a high-density polyethylene crystallized from a stress melt by a calender method was investigated by means of rheo-optical techniques, such as simultaneous measurements of dynamic X-ray diffraction and birefringence with dynamic mechanical responses, in order to assign the $\alpha$ and possibly the $\beta$ mechanical dispersions of polyethylene.

First, the crystalline morphology of the calendered

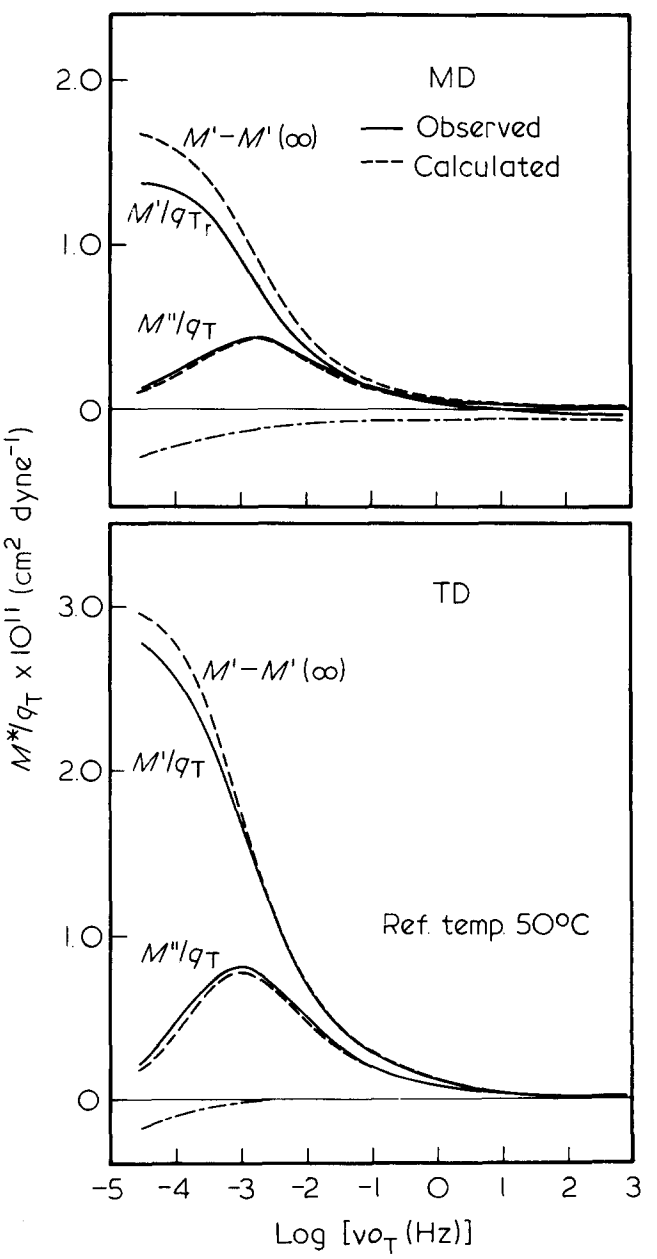


*Figure 22* Comparison of the calculated and observed complex dynamic stress–optical coefficient functions for the MD and TD specimens

specimen and its deformation mechanism during stretching the specimen up to an extension ratio of 1.4 along the machine direction (MD) of fabrication were investigated by electron microscopy, small-angle X-ray scattering and wide-angle X-ray diffraction. The morphology was revealed as the so-called row-nucleated crystalline texture of highly oriented cylindrites within which the crystal lamellae grown radially are stacked with their crystal *b*-axes (lamellar axes) highly perpendicular but their crystal *a*-axes rather parallel to the MD of fabrication. The deformation mechanism of the crystalline texture was explored in terms of the combinations of lamellar detwisting process to rotate the lamellar segments or crystal grains within the lamellae about their own crystal *b*-axes with lamellar splaying and bending processes at initial stage of stretching and, eventually, with lamellar tilting process to rotate the lamellar segments or the crystal grains about their own crystal *a*-axes, all so as to orient the crystal *c*-axes towards the stretching direction.

The tensile complex dynamic compliance function $J^*$ shows two dispersions classified as $\alpha_1$ and $\alpha_2$ mechanical retardation processes with activation energies of about 21 and 35 kcal $mol^{-1}$, respectively, not only for the MD specimen but for the specimen along transverse direction (TD) of fabrication. The complex dynamic stress–optical coefficient function $M^*$ exhibits, however, a single discrete dispersion designated as $\alpha$ optical retardation process with activation energy of about 24 kcal $mol^{-1}$ for both MD and TD specimens over the same frequency and temperature ranges covered for the dynamic mechanical measurements. The real and imaginary components of $M^*$ converge from positive values to almost zero at highest frequencies and lowest temperatures covered for both specimens, with an exception of the real component of the MD specimen which converges to a small but definitely negative value. The analysis of this unusual optical dispersion of the MD specimen in terms of the optical retardation time spectrum has ascribed the negative convergence to a negative form birefringence that arises from dynamic lamellar splaying or bending process responding quite in phase with dynamic bulk stress.

Finally, the dynamic X-ray diffraction studies for the specimens, especially for the MD specimen in terms of the complex dynamic orientation distribution function of crystallites (crystal grains) $\Delta w^*(\xi,0,\eta)$, have revealed the $\alpha$ optical dispersion and possibly the $\alpha$ mechanical dispersion to be mostly attributed to the crystal orientation dispersions involving intralamellar shearing processes, i.e. the detwisting and tilting processes of the lamellar segments or the crystal grains within the lamellae for the MD and TD specimens, respectively. The optical dispersion associated with the lamellar splaying or bending process to yield the negative form birefringence, if any, may be expected at higher frequencies or lower temperatures than those covered here to assign the $\beta$ mechanicaal dispersion to the interlamellar shearing process.

Judging from the particular crystalline texture of highly oriented cylindrites in the present row-nucleated specimen, the mechanical and optical responses of the MD and TD specimens must be representative of those at the equatorial and polar zones of the spherulitic specimen, and be serviceable enough to assign the $\alpha$ and $\beta$ mechanical dispersions of spherulitic polyethylene to the intra- and interlamellar crystal-grain-boundary phenomena, respectively.

## ACKNOWLEDGEMENTS

This series of rheo-optical studies on the deformation mechanism of semicrystalline polymers has been supported in part by a grant from the US–Japan Cooperative Research Program of the National Science Foundation, USA, and the Japan Society for Promotion of Science. The authors are also indebted to the Nippon Gosei Kagaku Co. Ltd, Osaka, Japan, and the Dai-Cell Chemical Industries Ltd, Osaka, Japan, for financial support through a scientific grant.

## REFERENCES

1 Kyu, T., Yasuda, N., Suehiro, S., Nomura, S. and Kawai, H. *Polym. J.* 1976, **8**, 565
2 Suehiro, S., Yamada, T., Inagaki, H., Kyu, T., Nomura, S. and Kawai, H. *J. Polym. Sci., Polym. Phys. Edn.* 1979, **17**, 763
3 Suehiro, S., Kyu, T., Fujita, K. and Kawai, H. *Polym. J.* 1979, **11**, 331
4 Suehiro, S., Yamada, T., Kyu, T., Fujita, K., Hashimoto, A. and Kawai, H. *Polym. Eng. Sci.* 1980, **19**, 929
5 Kyu, T., Yasuda, N., Suehiro, S., Hashimoto, T. and Kawai, H. *Polymer* 1980, **21**, 1205
6 Kyu, T., Suehiro, S., Nomura, S. and Kawai, H. *J. Polym. Sci., Polym. Phys. Edn.* 1980, **18**, 951
7 Kyu, T., Suehiro, S. and Kawai, H. *Polym. J.* 1980, **12**, 251
8 Kyu, T., Yamada, M., Suehiro, S. and Kawai, H. *Polym. J.* 1980, **12**, 809
9 Fujita, K., Suehiro, S., Nomura, S. and Kawai, H. *Polym. J.* 1982, **14**, 545
10 Nomura, S., Asanuma, A., Suehiro, S. and Kawai, H. *J. Polym. Sci. A-2* 1971, **9**, 1991
11 Nomura, S., Matsuo, M. and Kawai, H. *J. Polym. Sci., Polym. Phys. Edn.* 1972, **10**, 2489
12 Nomura, S., Matsuo, M. and Kawai, H. *J. Polym. Sci., Polym. Phys. Edn.* 1974, **12**, 1371
13 Sasaguri, K., Hoshino, S. and Stein, R. S. *J. Appl. Phys.* 1964, **35**, 47
14 Sasaguri, K., Yamada, R. and Stein, R. S. *J. Appl. Phys.* 1964, **35**, 3188
15 Oda, T., Nomura, S. and Kawai, H. *J. Polym. Sci. A* 1965, **3**, 1993
16 Oda, T., Sakaguchi, N. and Kawai, H. *J. Polym. Sci. C* 1966, **15**, 223
17 Fujita, K., Niwa, H., Nomura, S. and Kawai, H. *J. Polym. Sci., Polym. Phys. Edn.* submitted
18 Suehiro, S., Yamada, T., Inagaki, H. and Kawai, H. *Polym. J.* 1978, **10**, 315
19 Wang, T. T. *J. Polym. Sci., Polym. Phys. Edn.* 1974, **12**, 145
20 Hashimoto, T., Prud'homme, R. E. and Stein, R. S. *J. Polym. Sci., Polym. Phys. Edn.* 1973, **11**, 709
21 Hashimoto, T., Nagatoshi, K., Todo, A. and Kawai, H. *Polymer* 1976, **17**, 1075
22 Hashimoto, T., Nagatoshi, K., Todo, A. and Kawai, H. *Polymer* 1976, **17**, 1063
23 Kyu, T., Yasuda, N., Tabushi, M., Nomura, S. and Kawai, H. *Polym. J.* 1976, **8**, 565
24 Ito, T., Oda, T., Kawai, H., Kawaguchi, T., Keedy, D. A. and Stein, R. S. *Rev. Sci. Instrum.* 1968, **39**, 1847
25 Roe, R. J. and Krigbaum, W. R. *J. Chem. Phys.* 1964, **40**, 2608
26 Krigbaum, W. R. and Roe, R. J. *J. Chem. Phys.* 1964, **41**, 737
27 Roe, R. J. *J. Appl. Phys.* 1965, **36**, 2024
28 Nomura, S. Kawai, H., Kimura, I. and Kagiyama, M. *J. Polym. Sci. A-2* 1970, **8**, 383
29 Sack, R. A. *J. Polym. Sci.* 1961, **54**, 543
30 Wilchinsky, Z. W. *J. Appl. Phys.* 1960, **31**, 1969
31 Keller, A. and Machin, M. J. *J. Macromol. Sci. B* 1967, **1**, 41
32 Nakayasu, H., Markovitz, H. and Plazek, D. J. *Trans. Soc. Rheol.* 1961, **5**, 261
33 Hoffman, J. D., Williams, G. and Passglia, E. *J. Polym. Sci. C* 1966, **14**, 173
34 Shimomura, A., Suehiro, S. and Kawai, H. *Rep. Prog. Polym. Phys., Jpn* in press; *J. Polym. Sci., Polym. Phys. Edn.* to be submitted